Journal of Colloid and Interface Science 606 (2022) 518–525

Contents lists available at ScienceDirect

Journal of Colloid and Interface Science

journal homepage: www.elsevier.com/locate/jcis

Boosting oxygen evolution activity of nickel iron hydroxide by iron hydroxide colloidal particles

Qiang Li [a], Ting He [a], Xingxing Jiang [a], Yulai Lei [a], Qiming Liu [b], Chuntai Liu [c], Zhifang Sun [a,*], Shaowei Chen [b,*], Yi Zhang [a,*]

[a] Hunan Provincial Key Laboratory of Micro & Nano Materials Interface Science, College of Chemistry and Chemical Engineering, Central South University, 932 Lushan South Road, Yuelu District, Changsha 410083, China
[b] Department of Chemistry and Biochemistry, University of California, 1156 High Street, Santa Cruz, CA 95064, USA
[c] Key Laboratory of Materials Processing and Mold, Ministry of Education, Zhengzhou University, Zhengzhou 450002, China

GRAPHICAL ABSTRACT

Adsorption of $Fe(OH)_3$ colloids onto NiFeOH significantly enhances the OER activity, likely as a result of charge transfer from Ni^{2+} to Fe^{3+} that facilitates the adsorption of key oxygen intermediates.

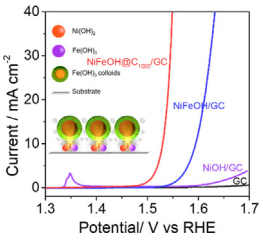

ARTICLE INFO

Article history:
Received 29 June 2021
Revised 27 July 2021
Accepted 5 August 2021
Available online 8 August 2021

Keywords:
Oxygen evolution reaction
Electrodeposition
Nickel iron hydroxide
Iron hydroxide colloidal particle
Electron-transfer

ABSTRACT

Nickel iron hydroxides (NiFeOH) have been drawing enormous attention as effective catalysts for oxygen evolution reaction (OER), a key process in water splitting. Herein, we report that negatively charged iron (III) hydroxide colloidal particles, can significantly enhance the OER activity of NiFeOH in alkaline media. NiFeOH is grown on nickel foam in a supersaturated iron(III) salt solution, which also contains a high content of $Fe(OH)_3$ colloidal nanoparticles, forming free-standing NiFeOH@C_x electrodes (with x being the Fe $(OH)_3$ concentration). The interface between NiFeOH and $Fe(OH)_3$ colloidal particles, as manifested by the unique volcano-like holes on the NiFeOH@C_x surface, is likely the OER active sites. In comparison to Fe $(OH)_3$-free NiFeOH, NiFeOH@C_{1000} exhibits a 40-fold enhancement of the OER activity, confirming the significant effect of $Fe(OH)_3$ colloidal nanoparticles in boosting the OER activity, likely as a result of enhanced charge transfer from Ni^{2+} to Fe^{3+} that facilitates the adsorption of key reaction intermediates. Furthermore, by coupling the free-standing NiFeOH@C_{1000} electrode with commercial Pt/C, full water splitting can occur and reach a current density of 10 mA cm^{-2} under a cell voltage of 1.51 V, which is lower than that (1.59 V) based on noble metal catalysts of RuO_2 + Pt/C.

1. Introduction

Water splitting has emerged as an effective technology in producing sustainable and clean energy by transforming intermittent

* Corresponding authors.
E-mail addresses: allensune@gmail.com (Z. Sun), shaowei@ucsc.edu (S. Chen), yzhangcsu@csu.edu.cn (Y. Zhang).

https://doi.org/10.1016/j.jcis.2021.08.037
0021-9797/

energies (e.g., solar and wind) into hydrogen fuel [1–7]; yet the efficiency is largely limited by the sluggish electron-transfer kinetics of oxygen evolution reaction (OER) at the anode [8,9]. Currently, leading OER catalysts are based on noble metals, such as Ir and Ru, and first-row transition metals (e.g., Ni, Fe, and Co) have been attracting enormous attention as viable alternatives, thanks mostly to their low costs, high abundance and competitive electrocatalytic activity [10–17]. Among these, nickel iron hydroxide (NiFeOH) catalysts have been found to display the highest activity in alkaline media [10,18,19]. However, the catalytic mechanism of NiFeOH has been under active debate. In particular, how iron promotes the electrocatalytic activity has remained largely elusive.

Recently, the high oxidation states of the Fe [20,21] and Ni [22] centers, as well as the synergistic interactions of Fe/Ni oxyhydroxides [23] have been put forward to account for the excellent activity. In addition, it has been reported that the OER activity of FeM (oxy)hydroxide clusters exhibits a linear correlation with the iron surface coverage, suggesting the importance of surface Fe species in OER electrocatalysis [24]. This can be impacted by "iron impurities" in the electrolytes in the form of free ions (within the concentration range of ppb to ppm). Another form of surface Fe species may arise from $Fe(OH)_3$ colloids, which can co-adsorb with metal ions onto the hydroxide surface; however the contribution of such adsorption to the OER activity has remained mostly unexplored thus far. Notably, theoretical calculations have confirmed that electronegative substrates [25], N sites [4], and phosphate groups [26] can promote the OER activity, because of partial withdrawal of electrons from the active centers. Within this context, $Fe(OH)_3$ colloids are anticipated to provide a large amount of electronegative surface Fe^{3+} and boost the OER activity of NiFe-based catalysts by a similar electron-transfer effect. This is the primary motivation of the present works.

In this study, for the first time ever, it is demonstrated that the OER activity of NiFeOH can be markedly enhanced by the adsorption of negatively charged $Fe(OH)_3$ colloidal particles. Experimentally, a series of free-standing electrodes were fabricated in an alkaline electrolyte, whereby Fe^{3+} was in situ electrodeposited onto nickel foam (NF) in a 1 M KOH solution containing $FeCl_3$ at varied concentrations (x, μM), and denoted as NiFeOH@C_x (Scheme 1). Among the series, the NiFeOH@C_{1000} electrode displayed the highest Fe content and the best OER performance with an overpotential (η_{10}) of only +238 mV to reach the current density of 10 mA cm^{-2}.

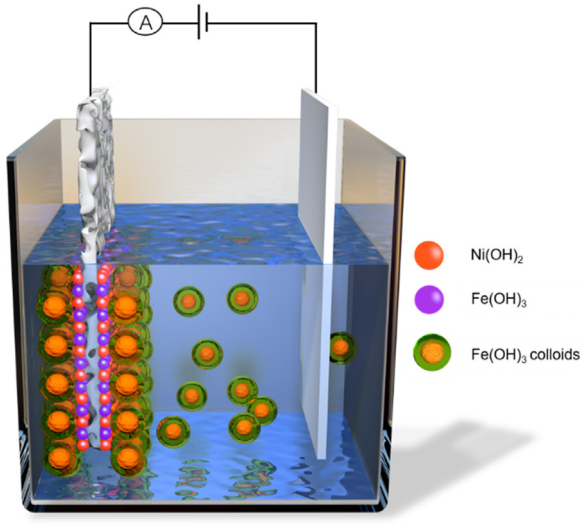

Scheme 1. Schematic illustration of the preparation of NiFeOH@C_x electrodes. The adsorption of negatively charged $Fe(OH)_3$ colloids onto the electropositive Ni/Fe centers is driven by electrostatic interaction.

The impact of $Fe(OH)_3$ colloids was further confirmed by comparing the OER activity of NiFeOH before and after modification with $Fe(OH)_3$ colloids, where the latter exhibited an OER activity about 40 times better than the former. X-ray photoelectron spectroscopic (XPS) studies indicate that the remarkable activity most probably arose from charge transfer from Ni^{2+} to Fe^{3+}, leading to an increase of the valence state of the Ni centers and hence enhanced adsorption of key oxygen intermediates. With the free-standing NiFeOH@C_{1000} electrode coupled with commercial Pt/C for water electrolysis, a cell voltage of 1.51 V was needed to reach the current density of 10 mA cm^{-2}, a performance better than that with commercial Pt/C + RuO_2 catalysts. This fundamental insight may be exploited for the design and engineering of efficient NiFe-based OER catalysts.

2. Experimental section

2.1. Materials

Ruthenium oxide (RuO_2, 99.9%) and 5 wt% Nafion solution were purchased from Sigma Aldrich (Shanghai, China). Potassium hydroxide (KOH), ferric chloride ($FeCl_3$), and nickel(II) chloride hexahydrate ($NiCl_2{\cdot}6H_2O$) were of analytical grade and purchased from Aladdin Reagents (Shanghai, China). Deionized water (18.2 MΩ cm) was supplied with a Barnstead water purification system. Beakers made of standard polystyrene (PE) were used instead of glass beakers during the tests unless otherwise specified.

2.2. Preparation of free-standing NiFeOH@C_x electrodes on nickel foam

Nickel foam (NF, 1 cm × 5 cm × 1.5 mm, bulk density 0.25 g cm^{-3}) was first sealed with an electronic sealant (displaying a working area of 1 cm^2), sonicated in 0.5 M H_2SO_4 for 10 min to remove the NiO_x layer on the surface, and then rinsed with water and ethanol. NiFeOH@C_x electrodes were then prepared by electrochemical deposition in a standard three-electrode set-up (Scheme 1), where the NF piece was used as the working electrode, a platinum plate as the counter electrode and Ag/AgCl (in saturated KCl) as the reference electrode. The electrolyte consisted of 1 M KOH, along with $FeCl_3$ at varying concentrations (e.g., x = 10, 100, and 1000 μM). The electrodeposition was carried out chronopotentiometrically at the current density of 10 mA cm^{-2} for 600 s, with the corresponding potential much higher than 1.23 V vs reversible hydrogen electrode (RHE), and the as-prepared electrodes were denoted as NiFeOH@C_{10}, NiFeOH@C_{100}, NiFeOH@C_{1000}, respectively.

2.3. Preparation of catalysts on a glassy carbon substrate

Experimentally, a glassy carbon (GC) electrode was sonicated in 0.5 M H_2SO_4 and rinsed with deionized water several times before use. NiOH was then electrodeposited onto the GC surface (NiOH/GC) from a 3 mM $Ni(NO_3)_2$ solution at a constant current of 0.02 mA for 300 s, corresponding to a thickness of about 20 nm [27]. NiFeOH/GC was then prepared by immersing the resultant NiOH/GC into a 40 mM $FeCl_3$ water solution for 5 min, where the solution showed no Tyndall effect. The obtained NiFeOH/GC electrode was rinsed with deionized water several times to remove residual iron ions, and immersed for 5 min in the $Fe(OH)_3$ colloid solution that contained 1 mM $FeCl_3$ in 1 M KOH, such that sufficient $Fe(OH)_3$ colloids were adsorbed onto the NiFeOH/GC electrode, producing NiFeOH@C_{1000}/GC.

For comparison, $Fe(OH)_3$ colloid/GC (denoted as C_{1000}/GC) was prepared at a Fe mass loading (12 μg/cm^2) equal to that of NiFeOH@C_{1000} by dropcasting a calculated amount of a solution

containing 1 mL of 1 mM $FeCl_3$ in 1 M KOH and 50 μL of 5 wt% nafion onto the GC surface.

2.4. Structural characterizations

Scanning electron microscopic (SEM) images were acquired on MIRA3 (LMH/LMU). X-ray powder diffraction (XRD) studies were carried out with an ADVANCE D8 diffractometer (Japan) using a graphite-filtered Cu K_α radiation at 40 kV. X-ray photoelectron spectra (XPS) were obtained with an ESCALAB 250Xi spectrometer (USA). Inductively coupled plasma mass spectrometry (ICP-MS) data were collected with an Agilent ICPMS 7700 instrument.

2.5. Electrochemistry

Voltammetric tests were performed on an RST 5200F electrochemical workstation (China). All electrochemical tests were carried out in a conventional three-electrode electrochemical cell. Oxygen-saturated 1 M KOH was used as the electrolyte solution. The NiFeOH@C_x supported on NF or GC prepared above were used as the working electrode, and a Pt plate as the counter electrode. The Ag/AgCl (in saturated KCl) reference electrode was calibrated against an RHE, and all potentials in the present study were referenced to this RHE [28]. Linear sweep voltammetry (LSV) was performed in 1 M KOH at the scan rate of 10 mV s^{-1}. The OER current density was obtained by normalizing the voltammetric current to the geometric area of the electrode, unless otherwise specified.

Before OER tests, cyclic voltammetry (CV) activation was conducted within the potential range of 1.0 to 1.6 V. Tafel slopes were measured from the OER polarization curves obtained at 0.1 mV s^{-1} in the KOH solution with 95% iR correction unless otherwise specified. Chronopotentiometry (CP) was used to investigate the stability of the NiFeOH@C_{1000} on NF at 10 mA cm^{-2} for OER, and the corresponding LSV curves were obtained before and after an aging test for 20 h. Electrochemical impedance spectroscopy (EIS) was tested at 1.5 V within the frequency range of 0.1 to 100 kHz.

Purification of KOH was prepared by following the Boettcher's method [27]. First, 2 g of $Ni(NO_3)_2{\cdot}6H_2O$, 4 mL of ultrapure H_2O, and 20 mL of 1 M KOH were added into a clean polypropylene centrifuge tube (50 mL). The tube was shaken and centrifuged, and the supernatant was carefully decanted. The washing cycle was repeated three times. Second, the tube was filled with 50 mL of 1 M KOH for purification. The solid was redispersed and mechanically agitated for at least 10 min, followed by at least 3 h of resting. The supernatant in the tube was the purified KOH and collected by centrifugation at 10,000 RPM for 5 min.

For the estimation of the electrochemical surface area (ECSA), the electrochemical double-layer capacitance (C_{dl}) of the catalysts was measured by CV measurements at a series of scan rates in the non-Faradaic potential range, and ECSA = C_{dl}/C_s with C_s being the specific capacitance of 0.040 mF cm^{-2} [29].

3. Result and discussion

$Ni(OH)_2$ can be readily generated by immersing a freshly polished NF in a KOH solution, and Fe^{3+} ions may react with local OH^- to form bimetallic hydroxide and deposit on the electrode surface [27,30]. Because of the ultralow solubility product of $Fe(OH)_3$ ($K_{sp} = 2.8 \times 10^{-38}$, 25 °C), only a trace concentration of free Fe^{3+} can be found in 1 M KOH. This suggests that iron impurities in alkaline solutions mainly exist in the form of colloidal particles rather than free ions.

Experimentally, an anodic current density of 10 mA cm^{-2} was applied to the NF electrode, corresponding to an initial potential of over 1.6 V vs RHE, to oxidize the Ni metal. $Fe(OH)_3$ colloids became visibly present when $FeCl_3$ was added into 1 M KOH at concentrations higher than 10 μM (Fig. 1**b**), and exhibited a zeta potential (ζ) of ca. −24 mV (100 μM $FeCl_3$), suggesting that the $Fe(OH)_3$ colloids were negatively charged (Fig. 1**a-d and S1**). This led to the co-adsorption of the colloidal nanoparticles onto the surface of positively charged NiFeOH to form NiFeOH@C_x. Meanwhile, negatively charged $Fe(OH)_3$ colloids might facilitate the adsorption of free Fe^{3+} residue in the electrolyte via electrostatic interaction, leading to enriched Fe^{3+} on the NiFeOH@C_x surface. In fact, the surface of the NiFeOH@C_x electrode can be seen to display a brown thin film after deposition (Fig. S2). SEM measurements show that the NiFeOH@C_{10} electrode displays a rough surface with a rather even distribution of nanoparticles (Fig. 1**e** and inset), in contrast to the smooth surface of bare NF (Fig. S3a and S3b) and NiFeOH@C_0 (Fig. S3c), suggesting the adsorption of $Fe(OH)_3$ colloidal particles from the electrolyte. For NiFeOH@C_{1000} that was prepared with a high $FeCl_3$ concentration, the number of colloidal particles significantly increased, along with the emergence of "volcano-like cavities", as highlighted by the red and white circles in Fig. 1**f** and inset. Note that the layer of $Fe(OH)_3$ colloids is not completely contiguous, likely due to the disruption of oxygen bubbles generated during continuous oxygen evolution. TEM measurements of the electrodeposited film scratched off from NF confirmed the formation of circular nanoparticles (Fig. 1**g**), which showed an average core diameter of about 3.2 nm (inset to Fig. 1**g**). Moreover, energy-dispersive X-ray spectroscopic (EDS) analysis confirmed that the nanoparticles are primarily composed of iron and oxygen (Fig. 1**h**), and the distributions of Fe and O are consistent with the dispersion of the nanoparticles. A trace amount of nickel was also found, due to electrostatic adsorption of nickel (from the NF) on the surface of the colloidal particles during ultrasonication. Taken together, these results suggest that $Fe(OH)_3$ colloidal particles were indeed formed on the NF surface. The nanoparticles displayed mostly amorphous structure (Fig. 1**i**), and XRD measurements show only the patterns of the nickel substrate, owing to the relatively low content of the active composites (details below) (Fig. S4).

In the process of sample preparation (Scheme 1), $Fe(OH)_3$ colloids were generated when $FeCl_3$ was added into the alkaline solution, and immediately deposited on the electrode surface. As the initial potential was over 1.6 V during the electrodeposition of $Fe(OH)_3$ colloids (Fig. S5), O_2 bubbles were produced at the interface between NiFeOH and $Fe(OH)_3$ colloidal particles, and led to partial removal of the colloidal particles and hence the generation of "volcano-like cavities" (Fig. 1**j**). Similar "volcano-like cavities" were also formed during the cooking of millet gruel (Video S1).

Notably, the surface morphologies varied significantly with the current density used in electrodeposition. For instance, when the current density was reduced to 2 mA cm^{-2} (NiFeOH@C_{1000}/2, vs NiFeOH@C_{1000} at 10 mA cm^{-2}), the production of oxygen bubbles was markedly diminished, and nanosheets were formed instead (Fig. 1**k** and **inset**), within which nanoparticles can be readily identified with a diameter almost the same as that of NiFeOH@C_{1000} (Fig. S6 and S7) and show an amorphous phase without lattice fringes.

The OER activity of the NiFeOH@C_x electrodes was then evaluated via LSV measurements (Fig. 2**a**). One can see that the activity varied markedly among the series of samples, with η_{10} = +424 mV for NiFeOH@C_0, +296 mV for NiFeOH@C_{10}, +267 mV for NiFeOH@C_{100}, and only +238 mV for NiFeOH@C_{1000}. That is, the OER activity increases markedly with the addition of an increasing concentration of $FeCl_3$. Notably, the NiFeOH@C_{1000} sample (+238 mV) even outperformed commercial RuO_2 (η_{10} = +309 mV) and was comparable to state-of-the-art NiFe-based catalysts (Fig. 2**e**, Table S1). The LSV curve of NiFeOH@C_{1000} was also

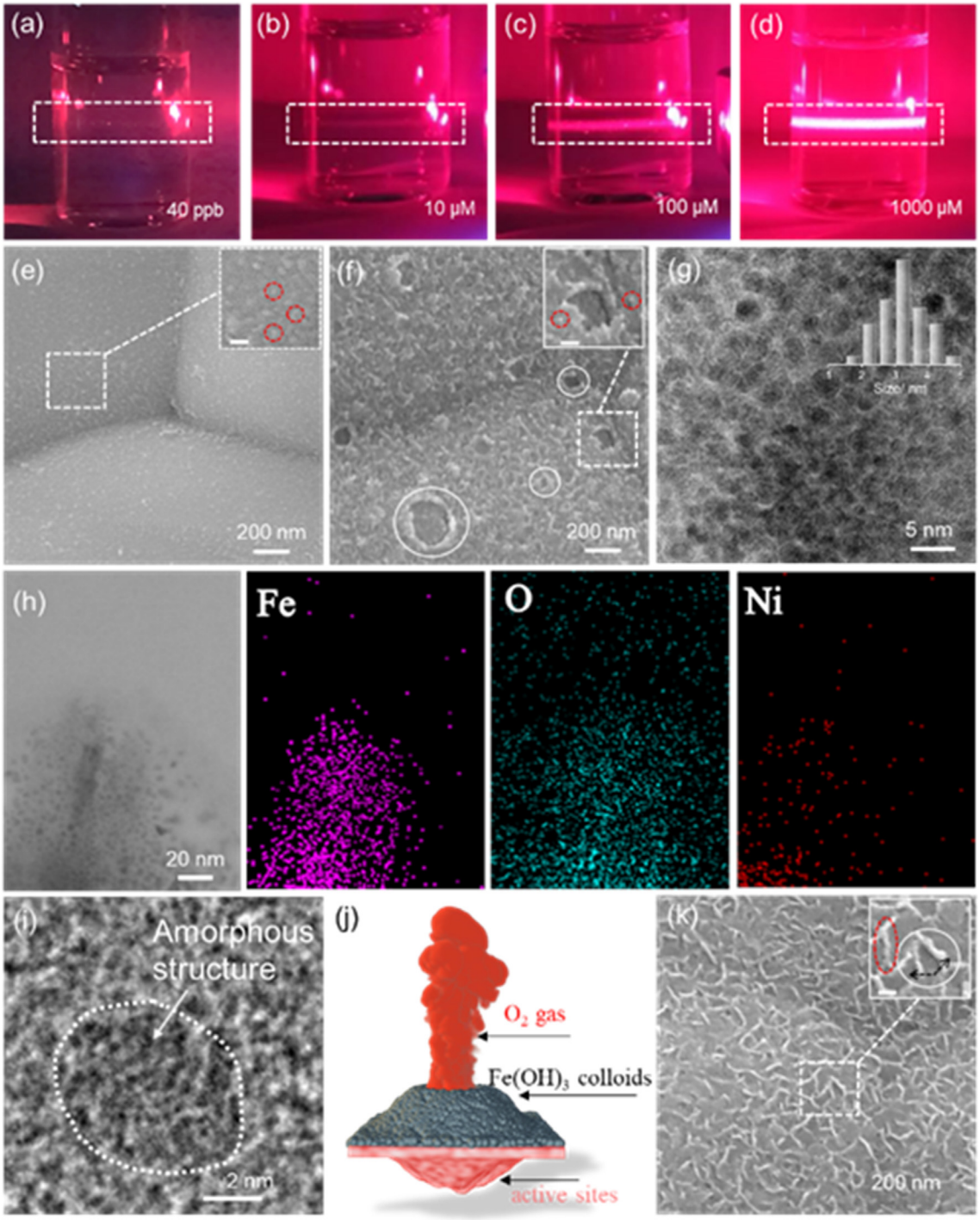

Fig. 1. Photographs of a $Fe(OH)_3$ colloid solution in 1 M KOH at varied Fe concentration: (a) < 40 ppb, (b) 10 μM, (c) 100 μM, and (d) 1000 μM. SEM images of (e) NiFeOH@C_{10} and (f) NiFeOH@C_{1000}. Insets are the corresponding zoom in of the box regions. The white circles are the volcano-like cavities and the red circles highlight the nanoparticles. (g) HRTEM image of $Fe(OH)_3$ colloids, which are peeled off from NiFeOH@C_{1000} by ultrasonication. Inset is the core size histogram. (h) HAADF-STEM image and corresponding EDS maps of $Fe(OH)_3$ colloids obtained as (g). (i) HRTEM image of a $Fe(OH)_3$ colloid. (j) Schematic illustration of volcano-like cavity derived from $Fe(OH)_3$ colloids. (k) NiFeOH@C_{1000}/2 prepared by electrodeposition at 2 mA cm^{-2} Inset is the zoom in of the dashed box.

recorded at a slow scan rate of 1 mV s^{-1} to diminish the influence of nickel oxidation on the determination of η_{10}. As shown in Fig. S8a, the Ni oxidation peak is significantly reduced, and there is only a negligible positive shift (4 mV) of η_{10}. Moreover, the NiFeOH@C_{100}/2 electrode exhibited an η_{10} of 241 mV, very close to that of NiFeOH@C_{1000} (+238 mV), indicating minimal impacts of the electrodeposition current density in electrode preparation on the eventual OER performance (Fig. S8b). In addition, the OER overpotentials of NiFeOH@C_{1000} at select current densities (i.e., 10, 50 and 100 mA cm^{-2}) estimated from the v-t curves (Fig. S8d) are very close to those from LSV measurements (Fig. 2**a**). Further experiments were conducted with electrodes prepared at the Fe^{3+} concentrations of 500 and 1500 μM. As displayed in Fig. S8c, the η_{10} value was essentially unchanged among the NiFeOH@C_{500}, NiFeOH@C_{1000} and NiFeOH@C_{1500} samples; yet, NiFeOH@C_{1000} can be seen to exhibit a somewhat better activity

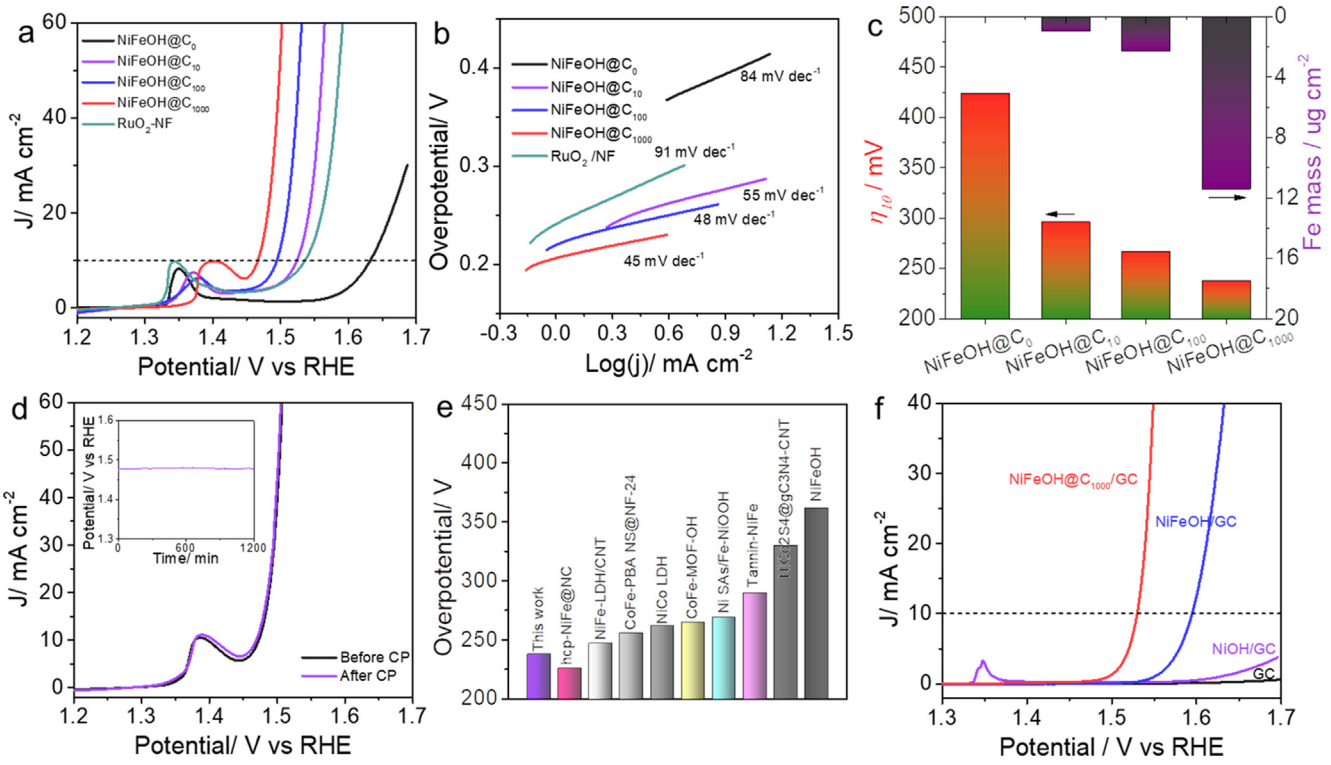

Fig. 2. (a) LSV curves and (b) Tafel plots of NiFeOH@C_x and RuO_2 electrodes in 1 M KOH. (c) Correlation between η_{10} and Fe content in NiFeOH@C_x samples. (d) OER polarization curves of NiFeOH@C_{1000} before and after the stability test. Inset shows the chronopotentiometric (CP) profile at the current density of 10 mA cm^{-2} for 20 h. (e) Comparison of η_{10} of NiFeOH@C_{1000} with leading transition metal-based catalysts reported recently in the literature. (f) Polarization curves of NiOH/GC, NiFeOH/GC, and NiFeOH@C_{1000}/GC in purified 1 M KOH.

at high current density than the other electrodes, suggesting that 1000 μM Fe^{3+} represented the optimal concentration for electrode preparation.

In addition, the ECSA of the NiFeOH@C_x electrodes displayed only a slight increase with increasing × (Fig. S9), suggesting that the enhanced OER performance of NiFeOH@C_{1000} arose from an improved intrinsic activity rather than an increase of the number of active sites. Notably, although the surface morphology of NiFeOH@C_{1000} is much rougher, it does not display a much larger ECSA, because the $Fe(OH)_3$ colloids is insulating under the measured potentials [31]. This also suggests that the actual active sites most likely resided at the interface between NiFeOH and $Fe(OH)_3$ colloids. The electrocatalytic activity of NiFeOH@C_x was also evaluated by normalizing the OER current to ECSA and compared to results of relevant transition metal-based catalysts reported recently (Table S2). It can be seen that NiFeOH@C_{1000} exhibited the highest current density (at 1.5 V vs RHE) among the NiFeOH@C_x catalysts, which was also over an order of magnitude higher than those of a number of catalysts reported earlier. This suggests that the intrinsic activity of NiFeOH@C_{1000} was enhanced by $Fe(OH)_3$ colloids through interfacial interactions.

Furthermore, NiFeOH@C_{1000} shows a Tafel slope of 45 mV dec^{-1}, which is much lower than other samples, indicating its fastest electron-transfer kinetics (Fig. 2**b**). Consistent results were obtained in EIS measurements, where the charge-transfer resistance (R_{ct}) was estimated to be 9 Ω for NiFeOH@C_{1000}, as compared to 12 Ω for NiFeOH@C_{100}, 15 Ω for NiFeOH@C_{10}, 67 Ω for NiFeOH@C_0 and 22 Ω for commercial RuO_2 (Fig. S10). Indeed, as shown in Fig. 2**c**, there is a positive correlation between the Fe content and OER activity of the NiFeOH@C_x samples. In addition, one can see a broad voltammetric peak within the range of 1.30 to 1.45 V, which is ascribed to Ni oxidation (Fig. 2a), and the NiFeOH@C_{1000} electrode displays a much more positive peak potential than other samples, likely due to enhanced adsorption of iron [27]. Remarkably, the OER polarization curves of NiFeOH@C_{1000} exhibited virtually no change after chronopotentiometric tests for 20 h, suggesting excellent stability (Fig. 2**d** and **inset**).

To unravel the significance of Fe additives in the OER electrocatalysis, a further control experiment was conducted. Experimentally, Fe impurity was removed from KOH [27], and a GC electrode was used instead of NF as the supporting substrate to minimize the interference of Fe residuals. NiOH was first electrodeposited onto the GC surface in a 3 mM $Ni(NO_3)_2$ solution (NiOH/GC) [30], and immersed into a $FeCl_3$ solution to prepare NiFeOH/GC, while NiFeOH@C_{1000}/GC was obtained by the adsorption of $Fe(OH)_3$ colloids onto NiFeOH/GC. From Fig. 2**f**, one can see that the NiOH/GC electrode displayed only a minimal activity towards OER, which was significantly improved with NiFeOH/GC, signifying the critical role of Fe additives in enhancing the OER activity, and even more so with NiFeOH@C_{1000}/GC, confirming the boosting effect of Fe $(OH)_3$ colloids on the OER activity. In fact, one can see that NiFeOH@C_{1000}/GC exhibited a 40-fold increase of the OER activity at +1.55 V as compared to NiFeOH/GC. However, $Fe(OH)_3$ colloids were unlikely the OER active sites, as the $Fe(OH)_3$ colloid/GC electrode displayed only a minimal activity (Fig. S11), largely because of the poor electrical conductivity of $Fe(OH)_3$ colloids [24,31].

Furthermore, the GC-supported electrodes exhibit an obvious change of the oxidation peak around 1.4 V, as compared to the NF-supported ones. Fig. S12a displays the zoom in of the polarization curves in this region (Fig. 2**f**). One can see that the oxidation peak disappeared with NiFeOH/GC, which could be accounted by the extensive doping of iron into NiFeOH [27,32]. Note that Fe in NiFeOH can be leached into the alkaline electrolyte, converted into $Fe(OH)_3$ colloids, and redeposited onto NiFeOH@C_{1000}/GC during the electrode preparation [24].

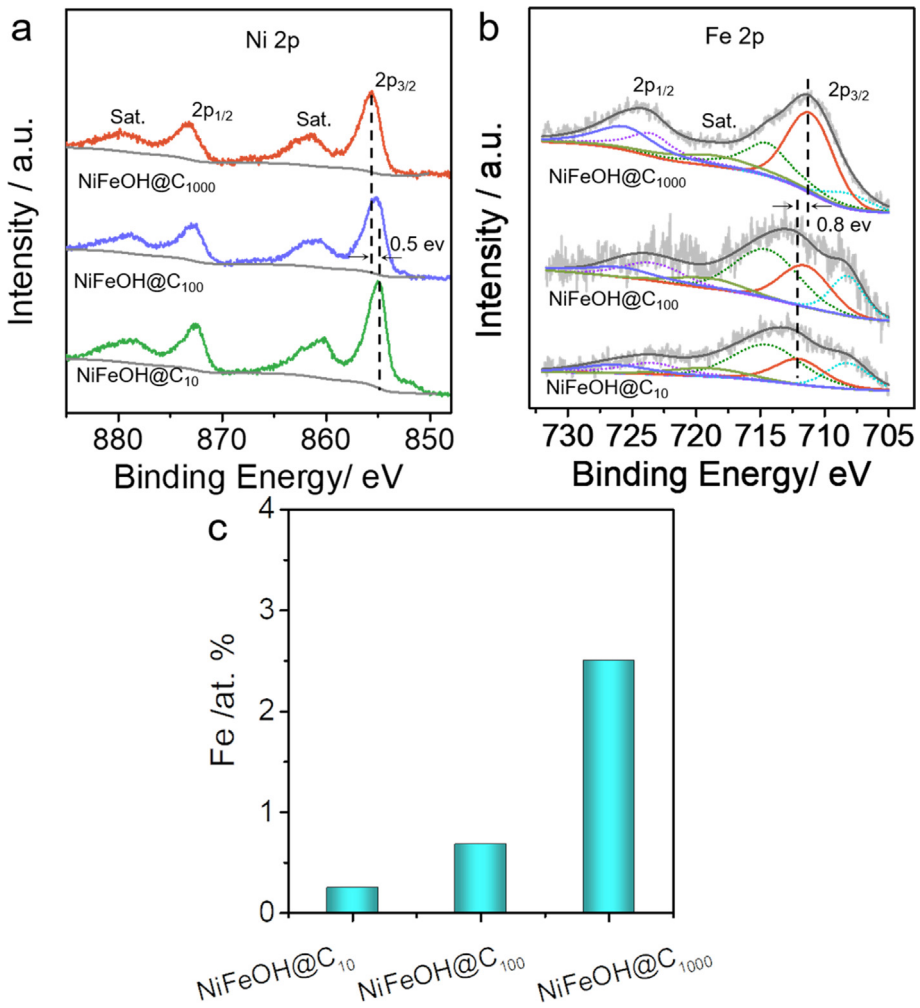

Fig. 3. XPS spectra of the (a) Ni 2p and (b) Fe 2p electrons in the NiFeOH@C_x sample series, and (c) the corresponding Fe contents (at%). The dot lines in (b) are derived from the Ni LMN spectra.

XPS measurements were then carried out to analyze the chemical composition, valence states, and electronic interactions of the series of catalysts deposited on NF (Fig. 3). First of all, based on the integrated peak areas, the Fe content was found to increase significantly from 0.25 at% for NiFeOH@C_{10} to 0.68 at% for NiFeOH@C_{100} and 2.15 at% for NiFeOH@C_{1000}, in accord with results from ICP-MS measurements (Fig. 3**c**), confirming the adsorption of Fe-rich nanoparticles onto the electrode surface. In contrast, a much smaller change was observed with the content of Ni (Table S3).

Fig. 3**a** shows the Ni 2p spectra of the three NiFeOH@C_x samples. For NiFeOH@C_{1000}, two peaks can be resolved at 855.6 and 873.3 eV, with a spin–orbit coupling of 17.7 eV, corresponding to the $2p_{3/2}$ and $2p_{1/2}$ electrons of Ni^{2+}, respectively [25]. In comparison, the Ni 2p binding energies for NiFeOH@C_{100} and NiFeOH@C_{10} are somewhat lower, at 855.3/872.8 eV, and 855.1/872.6 eV, respectively. This suggests increasingly electron-deficient nickel centers in the samples prepared at increasing $FeCl_3$ feed.

The Fe 2p spectra are shown in Fig. 3**b** (note that the overlapping spectra of Ni LMN have been removed [23]), where an opposite feature was observed. Two peaks can be deconvoluted at 711.1 and 725.5 eV for NiFeOH@C_{1000}, due to the $2p_{3/2}$ and $2p_{1/2}$ electrons of Fe^{3+}, respectively [30,33]. For comparison, the Fe 2p peaks of NiFeOH@C_{100} and NiFeOH@C_{10} are somewhat higher at 711.5/725.9 and 712.0/726.4 eV, respectively. This suggests electron transfer from Ni^{2+} to Fe^{3+}, which became intensified with increasing Fe^{3+} content in the catalyst [34–36]. The formation of electron-deficient nickel centers facilitated the transformation of insulating $Ni(OH)_2$ to conducting $Ni(OOH)_x$ [36,37], a critical step in the production of key OER intermediates, such as O* and OO* [34,38]. In addition, as O* intermediates could be stabilized by the high-valence Fe^{3+} sites, which lowered the energy barrier of OH* oxidation to O*, a potential limiting step in OER [39]. It is such synergistic interactions between Fe^{3+} and Ni^{2+} that led to the markedly enhanced OER activity.

Given the outstanding electrocatalytic activity towards OER, commercial Pt/C catalyst and NiFeOH@C_{1000} were combined to construct an overall water splitting system. As displayed in Fig. 4**a**, a low cell voltage (E_{10}) of 1.51 V was needed to reach the current density of 10 mA cm^{-2}, which is much improved as compared to that based on commercial noble metal catalysts RuO_2 +-Pt/C (1.59 V) and leading transition metal-based catalysts, such as Co_2P@Co_3O_4 (1.57 V) [40] and NiVB/rGO (1.56 V) [41]. One may also notice that the oxidation peaks of NiFeOH@C_{1000} + Pt/C and RuO_2 + Pt/C for water splitting appear to be obviously weaker than those observed in OER electrocatalysis (Fig. 2**a** and Fig. S12b). This is because LSV measurements were conducted with a three-electrode setup (with a stable reference), whereas water splitting was carried out in a two-electrode mode without a well-defined reference. There is no simple correlation between the numerical

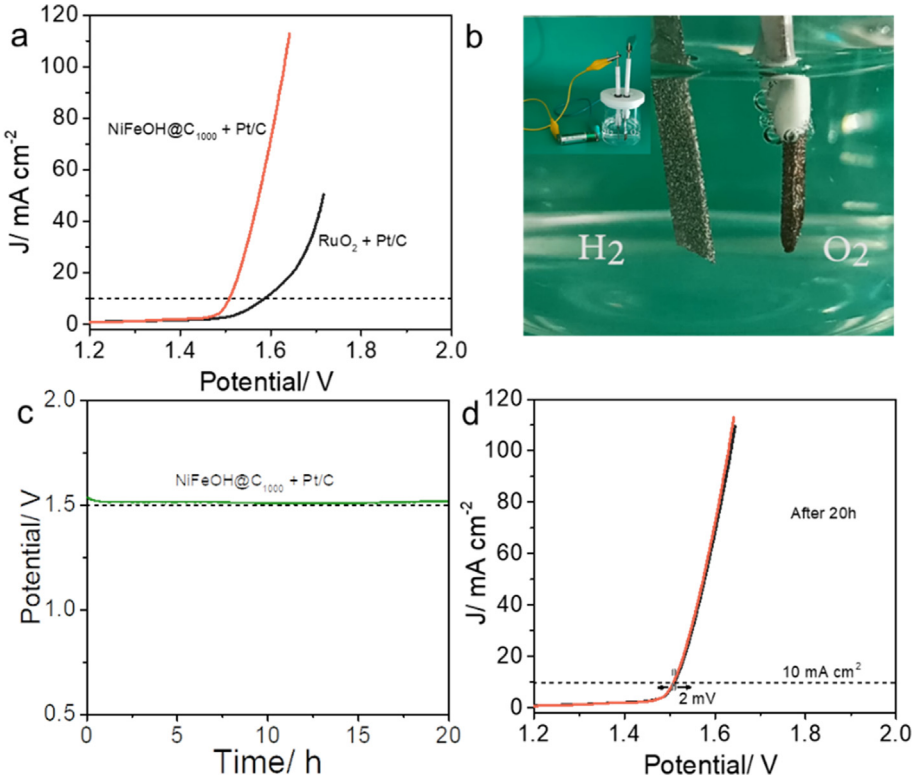

Fig. 4. (a) Polarization curves of overall water splitting by NiFeOH@C_{1000} + Pt/C and RuO_2 + Pt/C electrodes in 1 M KOH. (b) Digital photo of the NiFeOH@C_{1000} and Pt/C electrodes for water splitting. Inset shows the complete setup with one AA battery. (c) v-t curve of NiFeOH@C_{1000} + Pt/C for overall water splitting at the current density of 10 mA cm^{-2} for 20 h. (d) LSV curves of NiFeOH@C_{1000} + Pt/C for water splitting before and after the stability test in (c).

values in Fig. 2a and those in Fig. 4a. Such a behavior has been observed previously [42,43]. Fig. 4**b** and inset depict the digital photos of water splitting with one AA battery (1.5 V), and the formation of H_2 and O_2 bubbles can be clearly seen (Video S2). Moreover, the water splitting system can work continuously for over 20 h, and E_{10} remained virtually unchanged, demonstrating good stability and high potential of the NiFeOH@C_{1000} + Pt/C couple in overall water splitting (Fig. 4**c** and 4d).

4. Conclusion

In conclusion, the deposition of negatively charged $Fe(OH)_3$ colloids onto NiFeOH has been found to significantly enhance the OER performance by approximately 40 times, with the intrinsic activity over an order of magnitude better than those of leading transition metal-based catalysts. With the NiFeOH@C_{1000} + Pt/C system, a low cell voltage of 1.51 V was needed to power full water splitting at the current density of 10 mA cm^{-2}. The remarkable performance was primarily accounted by the negatively charged $Fe(OH)_3$ colloids that facilitated the adsorption and surface enrichment of Fe on the electrode as well as charge transfer from Ni^{2+} to Fe^{3+} that enhanced the adsorption of key oxygen intermediates and OER electron-transfer kinetics. Such a unique strategy is energy- and time-efficient, environmentally friendly, and may be exploited for the design and engineering of high-performance electrocatalysts based on transition metal hydroxides for a wide range of important reactions.

Declaration of Competing Interest

The authors declare that they have no known competing financial interests or personal relationships that could have appeared to influence the work reported in this paper.

Acknowledgments

This work was supported by the National Natural Science Foundation of China (21773311, 21972169, 21473257), Fundamental Research Funds for the Central Universities of Central South University (2019zzts125), and the Hunan Provincial Science and Technology Plan Project, China (2019TP1001). S. W. C. thanks the National Science Foundation (CHE-1900235) for partial support of the work.

Appendix A. Supplementary material

Supplementary data to this article can be found online at https://doi.org/10.1016/j.jcis.2021.08.037.

References

[1] Z.W. Seh, J. Kibsgaard, C.F. Dickens, I.b. Chorkendorff, J.K. Nørskov, T.F. Jaramillo, Combining theory and experiment in electrocatalysis: Insights into materials design, Science 355 (6321) (2017) eaad4998, https://doi.org/10.1126/science:aad4998.
[2] M.K. Debe, Electrocatalyst approaches and challenges for automotive fuel cells, Nature 486 (7401) (2012) 43–51.
[3] N.-T. Suen, S.-F. Hung, Q. Quan, N. Zhang, Y.-J. Xu, H.M. Chen, Electrocatalysis for the oxygen evolution reaction: recent development and future perspectives, Chem. Soc. Rev. 46 (2) (2017) 337–365.
[4] X. Han, W. Zhang, X. Ma, C. Zhong, N. Zhao, W. Hu, Y. Deng, Identifying the Activation of Bimetallic Sites in NiCo2S4@g-C3N4-CNT Hybrid Electrocatalysts for Synergistic Oxygen Reduction and Evolution, Adv. Mat. 31 (18) (2019) 1808281, https://doi.org/10.1002/adma.v31.1810.1002/adma.201808281.
[5] Q. Li, T. He, Y.-Q. Zhang, H. Wu, J. Liu, Y. Qi, Y. Lei, H. Chen, Z. Sun, C. Peng, L. Yi, Y.i. Zhang, Biomass Waste-Derived 3D Metal-Free Porous Carbon as a Bifunctional Electrocatalyst for Rechargeable Zinc-Air Batteries, ACS Sustain. Chem. Eng. 7 (20) (2019) 17039–17046.
[6] W. Yang, S. Chen, Recent progress in electrode fabrication for electrocatalytic hydrogen evolution reaction: A mini review, Chem. Eng. J. 393 (2020) 124726.

[7] Y. Wei, A. Liao, Y. Zhou, Z. Zou, Enhancing the water splitting performance via decorating Fe_2O_3 nanoarrays with oxygen-vacancy-rich $Ni_{1-x}Fe_xS$ electrocatalyst, Materials Today Physics 16 (2021) 100317.
[8] R.D. Smith, M.S. Prevot, R.D. Fagan, Z. Zhang, P.A. Sedach, M.K. Siu, S. Trudel, C. P. Berlinguette, Photochemical route for accessing amorphous metal oxide materials for water oxidation catalysis, Science 340 (2013) 60–63.
[9] T.R. Cook, D.K. Dogutan, S.Y. Reece, Y. Surendranath, T.S. Teets, D.G. Nocera, Solar energy supply and storage for the legacy and non legacy worlds, Chem. Rev. 110 (2010) 6474–6502.
[10] F. Song, L. Bai, A. Moysiadou, S. Lee, C. Hu, L. Liardet, X. Hu, Transition metal oxides as electrocatalysts for the oxygen evolution reaction in alkaline solutions: an application-inspired renaissance, J. Am. Chem. Soc. 140 (2018) 7748–7759.
[11] T. He, B. Lu, Y. Chen, Y. Wang, Y. Zhang, J.L. Davenport, A.P. Chen, C.-W. Pao, M. Liu, Z. Sun, A. Stram, A. Mordaunt, J. Velasco, Y. Ping, Y. Zhang, S. Chen, Nanowrinkled carbon aerogels embedded with fenx sites as effective oxygen electrodes for rechargeable zinc-air battery, Research 2019 (2019) 1–13.
[12] T. He, Y. Zhang, Y. Chen, Z. Zhang, H. Wang, Y. Hu, M. Liu, C.-W. Pao, J.-L. Chen, L.Y. Chang, Z. Sun, J. Xiang, Y.i. Zhang, S. Chen, Single iron atoms stabilized by microporous defects of biomass-derived carbon aerogels as high-performance cathode electrocatalysts for aluminum–air batteries, J. Mater. Chem. A 7 (36) (2019) 20840–20846.
[13] Y. Chen, S. Hu, F. Nichols, F. Bridges, S. Kan, T. He, Y.i. Zhang, S. Chen, Carbon aerogels with atomic dispersion of binary iron–cobalt sites as effective oxygen catalysts for flexible zinc–air batteries, J. Mater. Chem. A 8 (23) (2020) 11649–11655.
[14] Y. Li, F.-M. Li, X.-Y. Meng, S.-N. Li, J.-H. Zeng, Y.u. Chen, Ultrathin Co_3O_4 nanomeshes for the oxygen evolution reaction, ACS Catal. 8 (3) (2018) 1913–1920.
[15] K. Zeng, W. Li, Y.u. Zhou, Z. Sun, C. Lu, J. Yan, J.-H. Choi, R. Yang, Multilayer hollow $MnCo_2O_4$ microsphere with oxygen vacancies as efficient electrocatalyst for oxygen evolution reaction, Chem. Eng. J. 421 (2021) 127831, https://doi.org/10.1016/j.cej.2020.127831.
[16] R. Gao, D. Yan, Recent development of Ni/Fe-based micro/nanostructures toward photo/electrochemical water oxidation, Adv. Energy. Mater. 10 (11) (2020) 1900954, https://doi.org/10.1002/aenm.v10.1110.1002/aenm.201900954.
[17] R. Gao, H. Zhang, D. Yan, Iron diselenide nanoplatelets: Stable and efficient water-electrolysis catalysts, Nano Energy 31 (2017) 90–95.
[18] S. Lee, L. Bai, X. Hu, Deciphering iron-dependent activity in oxygen evolution catalyzed by nickel-iron layered double hydroxide, Angew. Chem. Int. Ed. 59 (21) (2020) 8072–8077.
[19] C. Roy, B. Sebok, S.B. Scott, E.M. Fiordaliso, J.E. Sørensen, A. Bodin, D.B. Trimarco, C.D. Damsgaard, P.C.K. Vesborg, O. Hansen, I.E.L. Stephens, J. Kibsgaard, I. Chorkendorff, Impact of nanoparticle size and lattice oxygen on water oxidation on $NiFeO_xH_y$, Nat. Catal. 1 (11) (2018) 820–829.
[20] N. Yu, W. Cao, M. Huttula, Y. Kayser, P. Hoenicke, B. Beckhoff, F. Lai, R. Dong, H. Sun, B. Geng, Fabrication of FeNi hydroxides double-shell nanotube arrays with enhanced performance for oxygen evolution reaction, Appl. Catal. B: Environ. 261 (2020) 118193, https://doi.org/10.1016/j.apcatb.2019.118193.
[21] D.A. Corrigan, R.S. Conell, C.A. Fierro, D.A. Scherson, In-situ Moessbauer study of redox processes in a composite hydroxide of iron and nickel, J. Phys. Chem. 91 (19) (1987) 5009–5011.
[22] X. Su, Y.u. Wang, J. Zhou, S. Gu, J. Li, S. Zhang, Operando spectroscopic identification of active sites in nife prussian blue analogues as electrocatalysts: Activation of oxygen atoms for oxygen evolution reaction, J. Am. Chem. Soc. 140 (36) (2018) 11286–11292.
[23] F. Song, M.M. Busch, B. Lassalle-Kaiser, C.-S. Hsu, E. Petkucheva, M. Bensimon, H.M. Chen, C. Corminboeuf, X. Hu, An unconventional iron nickel catalyst for the oxygen evolution reaction, ACS Central. Sci. 5 (3) (2019) 558–568.
[24] D.Y. Chung, P.P. Lopes, P. Farinazzo Bergamo Dias Martins, H. He, T. Kawaguchi, P. Zapol, H. You, D. Tripkovic, D. Strmcnik, Y. Zhu, S. Seifert, S. Lee, V.R. Stamenkovic, N.M. Markovic, Dynamic stability of active sites in hydr(oxy) oxides for the oxygen evolution reaction, Nat. Energy 5 (3) (2020) 222–230.
[25] W. Wang, Y. Lu, M. Zhao, R. Luo, Y.a. Yang, T. Peng, H. Yan, X. Liu, Y. Luo, Controllable tuning of cobalt nickel-layered double hydroxide arrays as multifunctional electrodes for flexible supercapattery device and oxygen evolution reaction, ACS Nano 13 (10) (2019) 12206–12218.
[26] Q. Hu, G.M. Li, X.F. Liu, B. Zhu, X.Y. Chai, Q.L. Zhang, J.H. Liu, C.X. He, Superhydrophilic phytic-acid-doped conductive hydrogels as metal-free and binder-free electrocatalysts for efficient water oxidation, Angew. Chem. Int. Edit. 58 (2019) 4318–4322.
[27] L. Trotochaud, S.L. Young, J.K. Ranney, S.W. Boettcher, Nickel-iron oxyhydroxide oxygen-evolution electrocatalysts: the role of intentional and incidental iron incorporation, J. Am. Chem. Soc. 136 (2014) 6744–6753.
[28] H. Li, S. Chen, X. Jia, B. Xu, H. Lin, H. Yang, L. Song, X. Wang, Amorphous nickel-cobalt complexes hybridized with 1T-phase molybdenum disulfide via hydrazine-induced phase transformation for water splitting, Nat. Commun. 8 (2017) 15377.
[29] C.C. McCrory, S. Jung, J.C. Peters, T.F. Jaramillo, Benchmarking heterogeneous electrocatalysts for the oxygen evolution reaction, J Am Chem Soc 135 (2013) 16977–16987.
[30] X. Lu, C. Zhao, Electrodeposition of hierarchically structured three-dimensional nickel-iron electrodes for efficient oxygen evolution at high current densities, Nat. Commun. 6 (2015) 6616.
[31] S. Zou, M.S. Burke, M.G. Kast, J. Fan, N. Danilovic, S.W. Boettcher, Fe (Oxy) hydroxide oxygen evolution reaction electrocatalysis: intrinsic activity and the roles of electrical conductivity, substrate, and dissolution, Chem. Mater. 27 (2015) 8011–8020.
[32] M.W. Louie, A.T. Bell, An investigation of thin-film Ni-Fe oxide catalysts for the electrochemical evolution of oxygen, J Am Chem Soc 135 (2013) 12329–12337.
[33] Q. Wu, J. Ouyang, K. Xie, L. Sun, M. Wang, C. Lin, Ultrasound-assisted synthesis and visible-light-driven photocatalytic activity of Fe-incorporated TiO2 nanotube array photocatalysts, J. Hazard. Mater. 199–200 (2012) 410–417.
[34] B. Fei, Z. Chen, J. Liu, H. Xu, X. Yan, H. Qing, M. Chen, R. Wu, Ultrathinning nickel sulfide with modulated electron density for efficient water splitting, Adv. Energy. Mater. 10 (2020) 2001963.
[35] J. Qi, W. Zhang, R. Xiang, K. Liu, H.Y. Wang, M. Chen, Y. Han, R. Cao, Porous Nickel-Iron Oxide as a Highly Efficient Electrocatalyst for Oxygen Evolution Reaction, Adv. Sci. 2 (2015) 1500199.
[36] R.D. Smith, M.S. Prevot, R.D. Fagan, S. Trudel, C.P. Berlinguette, Water oxidation catalysis: electrocatalytic response to metal stoichiometry in amorphous metal oxide films containing iron, cobalt, and nickel, J. Am. Chem. Soc. 135 (2013) 11580–11586.
[37] X. Su, Y. Wang, J. Zhou, S. Gu, J. Li, S. Zhang, Operando spectroscopic identification of active sites in nife prussian blue analogues as electrocatalysts: activation of oxygen atoms for oxygen evolution reaction, J Am Chem Soc 140 (2018) 11286–11292.
[38] N. Li, D.K. Bediako, R.G. Hadt, D. Hayes, T.J. Kempa, F. von Cube, D.C. Bell, L.X. Chen, D.G. Nocera, Influence of iron doping on tetravalent nickel content in catalytic oxygen evolving films, Proc. Natl. Acad. Sci. U. S. A. 114 (2017) 1486–1491.
[39] F. Dionigi, Z.H. Zeng, I. Sinev, T. Merzdorf, S. Deshpande, M.B. Lopez, S. Kunze, I. Zegkinoglou, H. Sarodnik, D.X. Fan, A. Bergmann, J. Drnec, J.F. de Araujo, M. Gliech, D. Teschner, J. Zhu, W.X. Li, J. Greeley, B.R. Cuenya, P. Strasser, In-situ structure and catalytic mechanism of NiFe and CoFe layered double hydroxides during oxygen evolution, Nat. Commun. 11 (2020) 2522.
[40] L. Yao, N. Zhang, Y. Wang, Y. Ni, D. Yan, C. Hu, Facile formation of 2D $Co_2P@Co_3O_4$ microsheets through in-situ toptactic conversion and surface corrosion: Bifunctional electrocatalysts towards overall water splitting, J. Power Sources 374 (2018) 142–148.
[41] M. Arif, G. Yasin, M. Shakeel, M.A. Mushtaq, W. Ye, X. Fang, S. Ji, D. Yan, Highly active sites of NiVB nanoparticles dispersed onto graphene nanosheets towards efficient and pH-universal overall water splitting, J Energy Chem 58 (2021) 237–246.
[42] J. Zhou, L. Yu, Q. Zhou, C. Huang, Y. Zhang, B.o. Yu, Y. Yu, Ultrafast fabrication of porous transition metal foams for efficient electrocatalytic water splitting, Appl. Catal. B: Environ. 288 (2021) 120002, https://doi.org/10.1016/j.apcatb.2021.120002.
[43] W. Ye, Y. Yang, X. Fang, M. Arif, X. Chen, D. Yan, 2D cocrystallized metal–organic nanosheet array as an efficient and stable bifunctional electrocatalyst for overall water splitting, ACS Sustain. Chem. Eng. 7 (21) (2019) 18085–18092.